

# Learning 3D-Gaussian Simulators from RGB Videos

Mikel Zhobro A. René Geist\* Georg Martius\*

University of Tübingen Max Planck Institute for Intelligent Systems, Tübingen

{mikel.zhobro, rene.geist, georg.martius}@uni-tuebingen.de

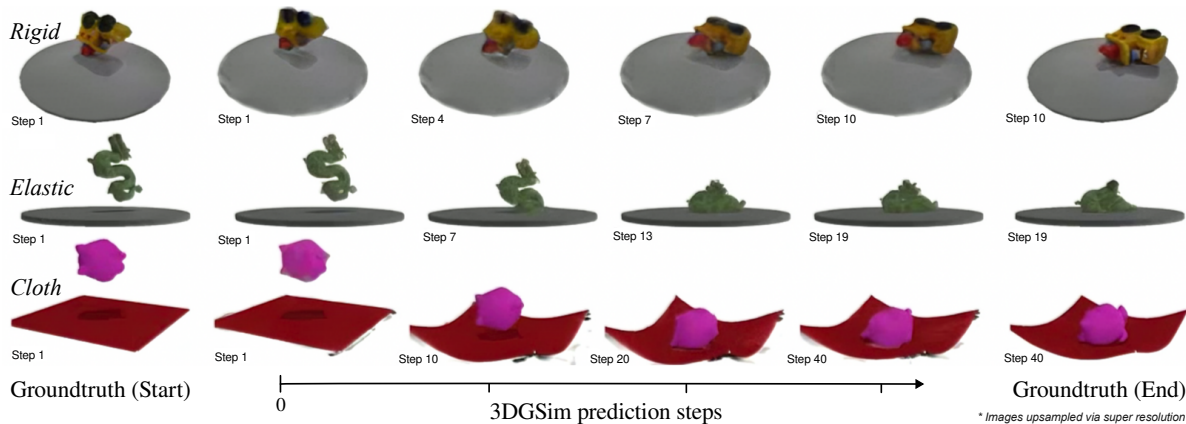


Figure 1. 3DGSim is a particle-based simulator that predicts scene dynamics from multi-view RGB images, leveraging recent advancements in point cloud transformers and 3D Gaussian scene representations. The predictions above showcase the model’s ability to capture deformations and shadows despite being trained on just 1,000 trajectories of six objects.

## Abstract

*Learning physics simulations from video data requires maintaining spatial and temporal consistency, a challenge often addressed with strong inductive biases or ground-truth 3D information – limiting scalability and generalization. We introduce 3DGSim, a 3D physics simulator that learns object dynamics end-to-end from multi-view RGB videos. It encodes images into a 3D Gaussian particle representation, propagates dynamics via a transformer, and renders frames using 3D Gaussian splatting. By jointly training inverse rendering with a dynamics transformer using a temporal encoding and merging layer, 3DGSim embeds physical properties into point-wise latent vectors without enforcing explicit connectivity constraints. This enables the model to capture diverse physical behaviors, from rigid to elastic and cloth-like interactions, along with realistic lighting effects that also generalize to unseen multi-body interactions and novel scene edits.*

## 1. Introduction

Video generation models [1–3] hold great promise for enabling robotic reasoning in unstructured environments. However, despite advances in visual realism, their predictions can sometimes lack physical plausibility [4], exhibit-

ing artifacts such as erratic object motion, unexpected shape changes, or lack of object permanence. These limitations reduce their reliability significantly, presenting a critical challenge for using these models in robot decision-making.

A strategy to enhancing a model’s physical accuracy is to embed physics-based inductive bias into its design. One realization of this idea involves utilizing a purely physics-based simulation combined with a learned mapping from images or text to the simulator’s state as in [12–15]. While physics simulators [16–22] are an indispensable tool for robotics, fully leveraging their potential requires precise state estimation and meticulous dynamics tuning. Moreover, as noted by [4], learning a simulator from vision necessitates capturing complex physical phenomena, including material mechanics, light transport, magnetism, fluid dynamics, and thermodynamics. In turn, each bias introduced into vision-based simulators risks becoming a constraint, potentially limiting the model’s ability to generalize across scenarios. This aligns with Rich Sutton’s conclusion in his “bitter lesson”: over decades of AI research, models emphasizing scalability and adaptability have consistently outperformed those relying on hand-crafted inductive biases and human-designed reasoning.

A promising direction to improve the physical accuracy of vision-based simulators are *particle-based simulators* (PBS) as shown in Table 1. Significant progress in

\*Equal advising.

Table 1. Overview on recently proposed particle-based simulators. While most works resort to a combination of kNN and GNNs, our work distinguishes itself from prior work by resorting to 3D-GS, space filling curves for point cloud serialization, and training the inverse rendering encoder alongside a dynamics transformer.

		Scene representation	Inverse renderer (☼: Solely pretrained)	Graph synthesis	Dynamics model	Forward rendering
<b>SDF-Sim</b>	[5]	Mesh	n.a.	SDF	GNN	n.a.
<b>Saleh et al.</b>	[6]	Mesh	n.a.	Mesh	GNN + Attention	n.a.
<b>3DIntphys</b>	[7]	Point clouds	NeRF + Point sampling ☼	kNN	GNN	NeRF
<b>FIGNet</b>	[8]	Mesh faces	n.a.	BVH	GNN	n.a.
<b>Robocraft</b>	[9]	Point clouds	n.a. (RGB-D)	kNN	GNN	NeRF
<b>VPD</b>	[10]	Point clouds	n.a. (RGB-D + UNet)	kNN	GNN	NeRF
<b>HD-VPD</b>	[11]	Point clouds	n.a. (RGB-D + UNet)	kNN	GNN + Transformer	NeRF
<b>DEL</b>	[12]	Point clouds	NeRF (GPF) ☼	kNN	GNN + DEM	NeRF
<b>3DGSim</b>	(Ours)	Gaussian splats	MVSplat	SFC	Transformer	3D-GS

language modeling has relied on identifying effective representation through learned token embeddings. Analogously, PBSs propose particles instead of pixels as a more suitable embedding for modeling dynamics. This approach is motivated by physical environments being inherently composed of atoms, whose interactions govern the appearance of a scene.

However, existing PBS structure point clouds using the k-nearest neighbors (kNN) algorithm and propagate information through graph neural networks (GNNs), introducing scalability limitations [11] and inductive biases that hinder learning. To address these challenges, we propose 3DGSim, a novel PBS framework that jointly trains inverse rendering and dynamics model directly from RGB images using 3D Gaussian splatting. Specifically, 3DGSim introduces the following key contributions:

- **Training on RGB video:** Avoiding access to meshes or depth cameras, 3DGSim learns particle interactions directly from multi-view RGB images by representing scenes as 3D Gaussian point clouds.
- **Point cloud serialization over kNN:** Instead of relying on kNN to identify spatially close points, 3DGSim leverages *temporal point cloud serialization*, significantly enhancing model scalability.
- **Temporal encoding and merging layer:** Replacing GNN-based message passing, 3DGSim utilizes *temporal encoding and merging* of serialized point clouds, allowing transformers to process unstructured point-cloud embeddings efficiently.
- **Inverse physics rendering:** 3DGSim jointly trains inverse rendering alongside the dynamics model, embedding motion priors directly into the 3D Gaussian representation while mapping these latent embeddings to splats only before rendering.
- **Open-source** datasets and code.

## 2. Related work

Given the vast scope of data-driven simulators, we focus on vision-based simulations of the real world using

particle-based representations. These particle-based simulators (PBS), as summarized in Table 1, vary in how they generate scene representations and in their approaches to propagating particles over time.

**Encoding and rendering scene representations** Common scene representations include point clouds (aka particles), meshes, signed distance functions (SDFs), neural radiance fields (NeRFs) [23], and 3D Gaussians (aka splats) [24]. Point clouds – being 3D points located near a scene’s objects – can be obtained directly from RGB-depth cameras as done in [9–11] or via inverse rendering. Notably, [10, 11] deploy U-Net [25] inspired encoder architectures to obtain pixel-wise features that are trained jointly with the dynamics model. As highlighted by [10], this joint training approach, in contrast to the independent training used in [1], enables the encoder to capture features that are relevant to the system’s dynamics. We consider this aspect crucial for the design of PBS, therefore also train the encoder alongside dynamics via MVSplat [26]. Many works [7, 9–12] on PBS resort to NeRFs for rendering images, which is an implicit representation that stores rendering cues in the weights of the neural network. In comparison, we represent visual information directly in the particle clouds as 3D Gaussians (aka splats). Splats are an explicit representation that yields high-fidelity renderings while also being significantly faster compared to NeRF-based ray casting [24].

**Using point connectivity for learning dynamics** While the physically grounded representation of PBS is its core strength, the unstructured nature of these point clouds in both spatial and temporal dimensions presents a major challenge. To connect points spatially, [6, 8] require object meshes to establish connectivity within objects. [8] resorts to the BVH [27] to connect faces between bodies. As tree search methods such as BVH are computationally expensive iterating over all vertices, [5] motivates learning an SDF for collision detection.

While meshes can be obtained from point clouds using

meshing algorithms [28], such algorithms are computationally expensive and do not solve the problem of connecting points between objects. Therefore, most PBS [7, 9–12, 29] resort to furthest-point-sampling (FPS) and k-nearest neighbors (kNN) for connecting neighboring particles and deploy graph neural networks (GNN) for predicting dynamics. However, kNN is expensive requiring a forward pass on  $KN$  particle-neighbor pairs with number of neighbors  $K$  and number of particles  $N$ . Furthermore, kNN connects particles only locally such that passing information through a graph requires many parsing steps. However, this approach is problematic for rigid bodies, for which instant changes in velocity require passing information through the whole graph in a single time step. Recent works [6, 11] suggests adding attention layers to efficiently pass information through the graph.

Also closely related is DEL [12], which uses the material point method as inductive bias. Naturally, this physics bias also limits its applicability for the many real-world physical phenomena that this model cannot capture. In addition, DEL requires small time steps for stability, incurs considerable per-step kNN computation costs, and relies on accurate velocity estimates.

In contrast to these approaches, we employ point cloud serialization using space-filling curves, effectively reducing the computational overhead associated with kNN. These serializations are fed to a sparse convolutional neural network to obtain patch-wise particle embeddings. Further, drawing inspiration from [6, 11], we employ PTv3 [30], a hierarchical UNet-like Point Transformer as dynamics model, avoiding physics biases. By performing patch-wise pooling followed by attention, we avoid using global graph nodes that could act as a bottleneck for passing particle-wise features.

**Tracking** Tracking and dynamics models serve distinct purposes in point cloud processing. Tracking focuses on estimating the current scene representation using *present* (and optionally *past*) images, often by identifying and following keypoints. In contrast, dynamics models predict future representations based on *past* observations, capturing the underlying physics that govern the scene’s motion. For instance, [31–34] employ Gaussian Splatting, primarily for keypoint tracking and modeling of static deformations as well as robot control [35–37].

### 3. 3DGSim

As illustrated in Figure 2, 3DGSim consists of three building blocks: (i) an *encoder* that maps multi-view RGB images to 3D Gaussian particles, (ii) a *dynamics model* that simulates the motion of the Gaussians through time, and (iii) a *renderer* that yields images from the Gaussians. These components are trained jointly end-to-end to perform image reconstruction.

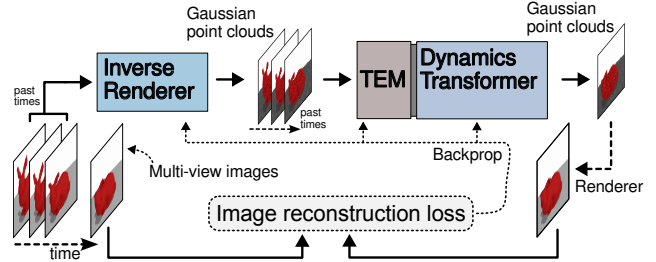


Figure 2. 3DGSim receives multi-view RGB images of the scene from  $T$  preceding time steps and is trained to predict the next image. First, an inverse renderer maps each set of images to 3D Gaussian point clouds. The Gaussian point clouds are then transformed by the dynamics transformer containing a temporal merging layer to predict a future point cloud. Finally, 3D-GS renders images from the predicted Gaussian point clouds.

#### 3.1. Forward rendering

3DGSim uses a 3D Gaussian point cloud representation which has been chosen to enable fast image rendering. Rendering is done using parts of the 3D Gaussian Splatting framework [24] which has emerged as an effective method for multi-view 3D image reconstruction, offering rapid inference, high fidelity, and the ability to edit scenes. Gaussian splatting uses a set of 3D Gaussian primitives, each parameterized by

$$g_i = (p_i, c_i, r_i, s_i, \sigma_i), \quad (1)$$

with the Gaussian’s mean  $p_i$  (aka particle position), its rotation  $r_i$ , spherical harmonics  $c_i$  (defining coloring), scale  $s_i$ , and opacity  $\sigma_i$ . To render novel views, these primitives are projected onto a 2D image plane using differential tile-based rasterization. The color value at pixel  $\mathbf{p}$  is calculated via alpha-blend rendering:

$$I(\mathbf{p}) = \sum_{i=1}^N \alpha_i c_i \prod_{j=1}^{i-1} (1 - \alpha_j)$$

where  $\alpha_i = \sigma_i e^{-\frac{1}{2}(\mathbf{p}-p_i)^\top \Sigma_i^{-1}(\mathbf{p}-p_i)}$  is the 2D density,  $I$  is the rendered image,  $N$  is the number of primitives in the tile, and  $\Sigma_i$  is the covariance matrix given by  $\Sigma_i = r_i s_i r_i^\top$  for improved computational stability.

#### 3.2. Inverse rendering encoder

As an encoder, we employ MVSpLat [26] to obtain a scene representation in form of 3D Gaussians. MVSpLat deploys a feed-forward network  $f_\phi$  with parameters  $\phi$  that maps  $M$  images  $\mathcal{I} = \{I^m\}_{i=m}^M$  with  $I^m \in \mathbb{R}^{(H \times W \times 3)}$  to a set of 3D Gaussian primitives

$$f_\phi : \{(I^m, P^m)\}_{m=1}^M \mapsto \{g_i\}_{i=1}^{M \times H \times W}.$$

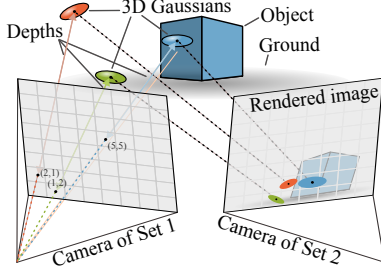


Figure 3. As encoder, we use MVsplat which estimates a 3D Gaussian splat for every image pixel in the first set of multi-view cameras. The Gaussians are estimated by projecting them onto the second set of cameras planes.

At each time step, MVsplat localizes Gaussian centers using a cost volume representation through plane sweeping and cross-view feature similarities. To do so, it requires the corresponding camera projection matrices  $\mathcal{P} = \{P^m\}_{m=1}^M$  which are calculated as  $P^m = K^m[R^m|t^m]$  via the matrices for the camera intrinsics and extrinsics  $K^m$ , rotation  $R^m$ , and translation  $t^m$ .

**Latent particle-wise features** Inspired by [11], we extend MVsplat to produce point-wise latent features

$$\tilde{g}_i = (p_i, f_i), \quad (2)$$

where the explicit rendering parameters typically associated with 3D Gaussian splatting  $g_i$  are replaced or supplemented by pixel-wise feature vectors  $f_i$ . These latent features capture latent scene properties and can optionally enrich the explicit representation  $g_i$ .

We defer the generation of explicit rendering parameters to the end of the pipeline, before rasterization. Specifically, we introduce a pixel-wise MLP that decodes latent features  $f_i$  into explicit 3DGS rendering parameters  $g_i$ . This allows the pixel-wise features  $f_i$  to better capture physics-related per-particle properties and avoids constraining the encoder with predicting only rendering-specific parameters.

MVsplat initially projects image-space parameters into the 3D world coordinate frame using camera intrinsics and estimated depth candidates, thus establishing accurate spatial scaling. Consequently, naive approaches for directly generating latent vectors  $\tilde{g}_i$  typically fail. Instead, we propose generating the pixel-wise latent features  $f_i$  via a dedicated MLP conditioned on projected parameters, depth, pixel shift, densities and geometric context captured through the Plücker coordinates of viewing rays:

$$\mathbf{r} = [\mathbf{o} \times \mathbf{d} \mid \mathbf{d}],$$

where  $\mathbf{o}$  and  $\mathbf{d}$  are the ray’s origin and direction, respectively [38]. The geometric encoding  $\mathbf{o} \times \mathbf{d}$  captures complex spatial relations otherwise challenging to parameter-

ize. Furthermore, our latent features  $f_i$  explicitly decompose into a dynamic component  $f_i^{\text{dyn}}$ , which the dynamics model can modify, and an invariant component  $f_i^{\text{inv}}$ , which remains fixed across all simulation steps. This decomposition provides flexibility, allowing the dynamics model to selectively update only  $f_i^{\text{dyn}}$ , while preserving  $f_i^{\text{inv}}$ . For clarity, even though we may subsequently refer simply to “updating  $f_i$ ” in the text, we always update exclusively the dynamic component  $f_i^{\text{dyn}}$ , leaving the invariant component  $f_i^{\text{inv}}$  unchanged.

**Masking background Gaussians** For each time step  $t_k$ , the encoder predicts for every image pixel a 3D Gaussian with latent feature  $\tilde{g}_i$ . In turn, for  $M$  images of size  $H \times W$  the total number of 3D Gaussians would amount to  $M \times H \times W$ . As not all Gaussian are equally important for predicting object motion as illustrated in Figure 3, Gaussians that belong to the scene’s background can be removed from the representation to save compute such that total number of Gaussian per point clouds amounts to  $N_k$ . Further, as done in [10], Gaussians that belong to static surfaces can be fed to the model but will not receive updates.

### 3.3. Dynamics transformer

The dynamics model predicts

$$\Delta p_T = p_{T+1} - p_T \text{ and } \Delta f_T = f_{T+1} - f_T, \quad (3)$$

given the past point clouds  $\{\{\tilde{g}_i(t_k)\}_{i=1}^{N_k}\}_{k=1}^T$ . As these point clouds are unstructured and vary in size at each time step due to the masking process, a fundamental challenge arises: *How can a network efficiently propagate the embedded physics information both spatially and temporally?* Given our primary objective of scaling models to learn particle dynamics from large datasets, we rely on PTv3 [30] which forms the current state of the art on representation learning with unstructured point clouds.

**Point cloud serialization** At the core of PTv3 lies “point cloud serialization”, an algorithm that transforms an unstructured point cloud into ordered points. This process begins by discretizing 3D space into a uniform grid of points. As illustrated in Figure 5, these point are then connected using a space-filling curve – a path that traverses each grid point exactly once while preserving spatial proximity as much as possible. Each point  $p_i$  is assigned an integer code  $s_i$ , representing its position within a space-filling curve, via the mapping

$$s_i = \phi^{-1}(\lfloor p_i/G \rfloor) \quad (4)$$

with  $\phi^{-1} : \mathcal{Z}^N \mapsto \mathcal{Z}$  and grid size  $G \in \mathbb{R}$ . The points in the clouds are then ordered by their respective code  $s_i$ , yielding a serialized point cloud (SPC)

$$S_i(t_k) = \{(s_i, \tilde{g}_i)\}_{i=1}^{N_k}. \quad (5)$$

While this approach may not preserve local connectivity as precisely as kNN groupings, [30] emphasizes that the slight loss in spatial precision is outweighed by a significant gain in computational efficiency. To obtain diverse spatial connections between points, PTV3 shuffles between four different space filling curve patterns to obtain SPCs from which patches are computed and varies the patch computation through integer dilation.

**Patch grouping** PTV3 partitions the SPC  $S_i(t_k)$  into equally sized patches and applies self-attention within each patch. To ensure divisibility, patches that do not align with the specified size are padded by borrowing points from neighboring patches.

**Conditional embeddings and patch attention** Besides the computational efficiency of SPC over kNN, its main advantage lies in the compatibility with standard dot-product attention mechanisms. To understand this, we first examine how the standard PTV3 architecture computes particle-wise predictions from a single point cloud at a single time step. The process begins by extracting particle-wise embeddings  $E_i$  for each serialized point  $(s_i, \tilde{g}_i)$  using a sparse convolutional neural network (CNN). Next, the embedded SPCs are progressively down sampled via grid pooling before being grouped and shuffled into patch pairs. Conditional positional embeddings (xCPE) are then added to the embeddings, followed by layer normalization and a patch-wise attention layer predicting the change in the embeddings  $\Delta E_i$ . The pooling, patch shuffling, and attention blocks are arranged in a U-net [25] like architecture that first reduces the size of the SPCs in an encoding step and then mirrors this architecture. In 3DGSim, the final layer of the dynamics model predicts the change in the particle positions  $\Delta p_i$  and the change in their features  $\Delta f_i$ .

**Temporal point cloud serialization** For dynamics prediction, we generate multiple latent particle clouds from different time steps  $t_1, \dots, t_T$  which are then transformed into SPCs by PTV3’s initialization block. To encode the time step  $t_k$  into the SPC, we extend the batch-version of the serialization (4) to

$$\tilde{s}_i(t_k, b) = \left[ \underbrace{b}_{(64 - \tau - \kappa) \text{ Bits}} \mid \underbrace{s_{t_k}}_{\tau \text{ Bits}} \mid \underbrace{s_i}_{\kappa \text{ Bits}} \right] \quad (6)$$

with batch size  $b$ , the temporal integer code  $s_{t_k}$ , total time step integer  $\tau = \log_2(T)$ , and  $\kappa = 48$  Bits. As each position dimension is encoded using 16 bits and using a grid size of  $G = 0.004$  m, the theoretical encoding capacity corresponds to a spatial extent of approximately  $0.004 \text{ m} \cdot 2^{16} \approx 216 \text{ m}$  per dimension. In turn, by extending PTV3’s initialization, we obtain the temporally serialized point clouds (t-SPC)  $\tilde{S}_i(t_k) = \{(\tilde{s}_i, \tilde{g}_i)\}_{i=1}^{N_k}$ .

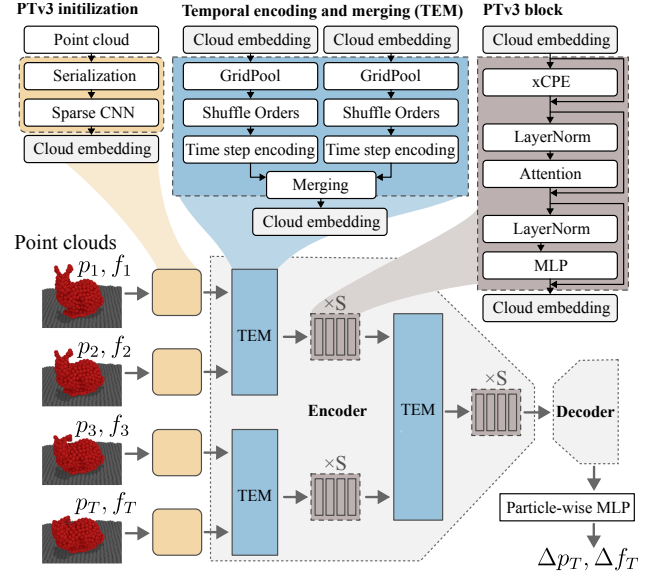


Figure 4. The dynamics model encodes the time step into each embedding and merges embeddings from adjacent time-steps. The TEM and PTV3 blocks are applied repeatedly until all embeddings are merged.

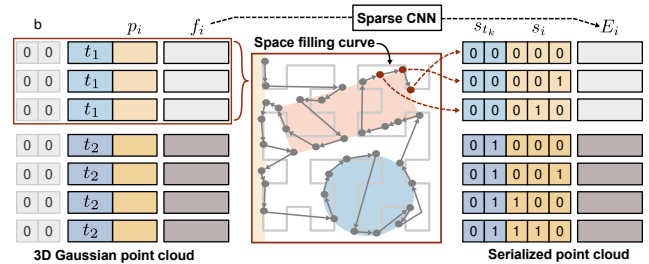


Figure 5. Temporal point cloud serialization.

**Temporal encoding** As shown in Figure 6, prior to merging point clouds from different time steps, we incorporate a learned, time-step-specific positional encoding  $E_{t_k}$  into the embeddings. Specifically, each embedding  $E_i(t_k)$  at time step  $t_k$  is updated as follows:

$$E_i(t_k) \leftarrow E_i(t_k) + E_{t_k}. \quad (7)$$

This temporal encoding ensures that the attention network can distinguish points across different temporal instances, enabling the model to reason about dynamics over time. Similar positional encoding methods have previously been applied in transformer architectures to differentiate positions within sequences [39].

**Temporal merging** Unlike PTV3, which limits attention computations exclusively to patches composed of points from the same time step within one batch, our method extends the receptive field across time steps. We achieve this

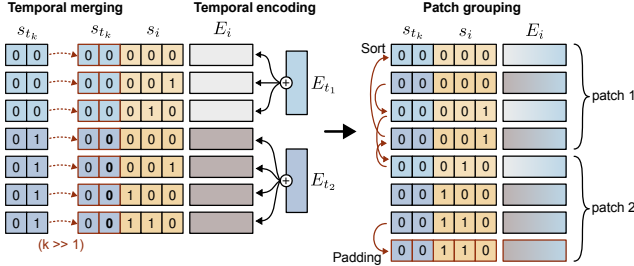


Figure 6. Temporal merging and embedding followed by patch grouping for the patch-wise attention mechanism.

by introducing a temporal merging operation, which applies a one-bit right shift to the temporal serialization codes  $s_{t_k}$ :

$$\text{Merge}(\tilde{s}_i) = [b \mid (s_{t_k} \gg 1) \mid s_i]. \quad (8)$$

For example, consider points initially serialized with temporal codes  $s_{t_1} = 0$  and  $s_{t_2} = 1$  as depicted in Figure 6. After temporal merging, the updated temporal codes become  $s_{t_1} = 0$  and  $s_{t_2} = 0$ . Thus, the points originally belonging to separate time steps now receive identical batch-temporal codes, enabling patch grouping to form patches that contain points from multiple time steps simultaneously. Consequently, our attention module can effectively model relationships among points across adjacent time steps within a single computational step.

In our current implementation, we specifically merge pairs of consecutive time steps  $t_j$  and  $t_{j+1}$ , where  $j \in 2n, n \in \mathbb{N}^*$ . We adopted this simple and computationally convenient strategy, though more sophisticated temporal merging schemes—such as merging points from larger windows of adjacent time steps—can also be explored in future work. Importantly, in contrast to [11], which require dedicated transformer modules for each time step, our temporal merging enables the reuse of the same attention block across time steps. This substantially reduces memory demands and facilitates greater knowledge transfer across time steps.

### 3.4. Loss function

3DGSim is trained solely on an image reconstruction loss. This loss is computed from rasterized multi-view images, generated based on both the encoder predictions of past point clouds  $\{\{g_i(t_k)\}_{i=1}^{N_k}\}_{k=0}^T$  and the simulated future point cloud trajectory  $\{\{g_i(t_k)\}_{i=1}^{N_k}\}_{k=T+1}^{T+T'}$ . Specifically, the loss is defined as:

$$\mathcal{L} = (1 - \lambda) \frac{1}{T} \sum_{k=0}^T \mathcal{L}_k + \lambda \sum_{k=T+1}^{T+T'} \gamma^k \mathcal{L}_k, \quad (9)$$

with  $\lambda = 0.5$ , temporal decay factor  $\gamma = 0.87$ ,  $T \in \{2, 4\}$  and  $T' = 12$ . The per-frame reconstruction loss  $\mathcal{L}_k$  mea-

Table 2. Comparison of 3DGSim to Cosmos. "Explicit" models use 3DGS parameters and a static latent feature as inputs to the dynamics model, while "Latent" models use only latent features mapped to Gaussians after dynamics. The †-model relaxes camera constraints (3 view cameras out of 6 total); the ‡-model omits segmentation masks for static elements. Metrics "future" and "past" are means over all timesteps. "4-12" denotes conditioning on 4 past states with rollout prediction of 12 future steps.

Dataset	Model	PSNR (future) ↑	PSNR (past) ↑
rigid	3DGSim 4-12 latent	<b>28.28 ± 2.52</b>	<b>32.93 ± 1.56</b>
	3DGSim 2-12 latent	28.08 ± 2.46	33.00 ± 1.62
	3DGSim 4-12 explicit	27.88 ± 2.43	32.77 ± 1.57
	3DGSim 2-12 explicit	27.07 ± 2.27	32.67 ± 1.65
	cosmos	22.35 ± 3.82	–
elastic	3DGSim 4-12 latent	<b>33.15 ± 3.51</b>	<b>34.55 ± 2.26</b>
	3DGSim 2-12 latent	32.05 ± 3.48	35.99 ± 1.88
	3DGSim 2-12 explicit	29.92 ± 1.72	40.85 ± 2.94
	3DGSim 4-12 explicit	29.69 ± 1.75	40.16 ± 3.07
	3DGSim 4-12 latent †	<b>31.60 ± 3.09</b>	<b>32.55 ± 2.12</b>
3DGSim 4-12 latent ‡	<b>32.66 ± 3.43</b>	<b>34.45 ± 2.44</b>	
cosmos	18.87 ± 3.99	–	
cloth	3DGSim 4-8 latent	<b>26.98 ± 2.63</b>	<b>34.81 ± 2.28</b>
	3DGSim 2-8 latent	26.25 ± 2.38	35.22 ± 1.97
	3DGSim 4-8 explicit	23.72 ± 1.52	39.75 ± 2.32
	3DGSim 2-8 explicit	17.97 ± 2.02	35.47 ± 1.68
	cosmos	21.10 ± 3.56	–

sures the discrepancy between ground-truth ( $I_k^{\text{gt}}$ ) and predicted ( $I_k$ ) multi-view images using a weighted combination of pixel-wise  $\ell_2$  and LPIPS [40] terms, reading

$$\mathcal{L}_k = \alpha \mathcal{L}_2(I_k^{\text{gt}}, I_k) + \beta \mathcal{L}_{\text{LPIPS}}(I_k^{\text{gt}}, I_k),$$

with hyper-parameters  $\alpha = 1$  and  $\beta = 0.05$ .

## 4. Experiments

In what follows, train 3DGSim on different datasets and test the model's ability to generalize.

**Model setup** Unless stated otherwise, the following training and parameter settings serve as defaults in the experiments. The **state** consists of dynamic  $f^{\text{dyn}}$  and invariant features  $f^{\text{inv}}$  of size (32, 32) for the implicit- and (0, 16) for the explicit 3D Gaussian particle representation. The **inverse rendering encoder** follows MVSplat, reducing candidate depths from 128 to 64 due to smaller scene distances. Default near-far depth ranges are [0.2, 4] for rigid bodies and [15, 8] for the other datasets. The **dynamics transformer** defaults to PTV3 with a 5-stage encoder (block depths [2,2,2,6,2]) and a 4-stage decoder ([2,2,2,2]). Grid pooling and temporal merging strides default to [1,4,2,2,2] and [1,2,2,2,2], respectively, with grid size  $G=0.004$  m. Attention blocks use patches of size 1024, encoder feature dimensions [32,64,128,256,512], decoder dimensions [64,128,256], encoder heads [2,4,8,16,32], and decoder

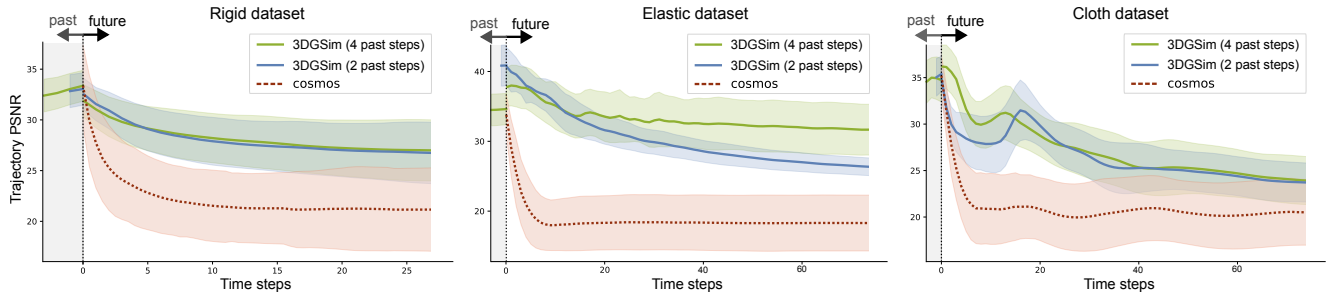


Figure 7. Comparison of our method to Cosmos. Cosmos is conditioned on the prompts: "A rigid body falling on a circular gray ground.", "A soft body falling on a circular-gray-ground." and "A rigid body falling on a red rectangular cloth which is fixed on its edges.". Metrics are computed on the same test images for all methods.

heads [4,4,8,16]. For the camera setup, we select 4 uniformly distributed views at random and an additional 5 target cameras from the remaining cameras (out of 12 total) to compute the reconstruction loss.

**Datasets** To evaluate 3DGSim’s robustness in learning dynamics from videos, we introduce three challenging datasets: rigid body, elastic, and cloth.

The rigid body dataset consists of 1,000 simulated trajectories involving six rigid objects (turtle, sonny school bus, squirrel, basket, lacing sheep, and turboprop airplane) from the GSO dataset [41]. Each trajectory spans 32 frames at 12 FPS, providing controlled dynamics characteristic of rigid body motion. The elastic dataset, aimed at capturing plastic deformable object dynamics, includes six objects (dragon, duck, kawaii demon, pig, spot, and worm) simulated using the Genesis MPM elastoplastic simulator [15]. Each object undergoes deformation upon collision with a circular gray ground, offering scenarios of complex elastic behavior. The cloth dataset includes the same set of objects as the elastic dataset. Here, the cloth is fixed at four corners, posing the challenge to infer implicit constraints and modeling dynamic cloth-like deformations. Both elastic and cloth datasets contain 200 trajectories per object, simulated with a time step of 0.001 and 20 substeps, resulting in 2-second sequences captured at 42 FPS (84 frames per trajectory).

**Metrics** For evaluation, 12% of trajectories are chosen at random and held out from each dataset, and we report each model’s PSNR (with SSIM being reported in the supplementary material). The PSNR (Peak Signal to Noise Ratio) correlates with the mean squared error between the ground truth and predicted images, and therefore captures both deviations in the dynamics and effects of blurring.

**Training** Our models are trained for ~120,000 steps using a cosine annealing warm-up and a learning rate of  $2 \times 10^{-4}$ , with batch sizes of 6 and 4 for 2-step and 4-step states, respectively. To optimize memory and speed, we use



Figure 8. 3DGSim’s prediction of a rigid plane captures shadows by adjusting the appearance of ground particles.

gradient checkpointing and flash attention v2 [42]. Training is performed on a single H100 GPU and typically takes 5 to 6 days to complete.

#### 4.1. Trajectory simulation

Figure 7 shows the PSNR of our model’s simulations using two or four past frames and the latent representation. To the best of our knowledge, 3DGSim is currently the only open-source, particle-based simulator trained directly on videos that integrates rendering and simulation; therefore, we compare against *Cosmos-1.0-Autoregressive-5B-Video2World* [3], a video generation model conditioned on 9-frame video input and language prompts. Additionally, we ablate key hyperparameters and report results in Table 2. Explicit representations achieve similar performance but generalize poorly, particularly with fewer cameras (see supplementary).

#### 4.2. Scene editing and model generalization

A key advantage of 3DGSim is its 3D representation of the simulator’s state, enabling direct scene editing for modular construction, counterfactual reasoning, and scenario exploration. By modifying object placements, adding elements, or altering physical properties, we test how the model adapts, demonstrating its flexibility and interpretability. To illustrate the model’s editability, we modified the height of the ground or removed it entirely – scenarios not encountered during training. Remarkably, the model adapts seamlessly, continuing to produce realistic simulations, which suggests a robust understanding of physics beyond its training distribution. For further demonstration, the interested reader is referred to the accompanying video.

As an additional rigorous test, we simulate multi-object

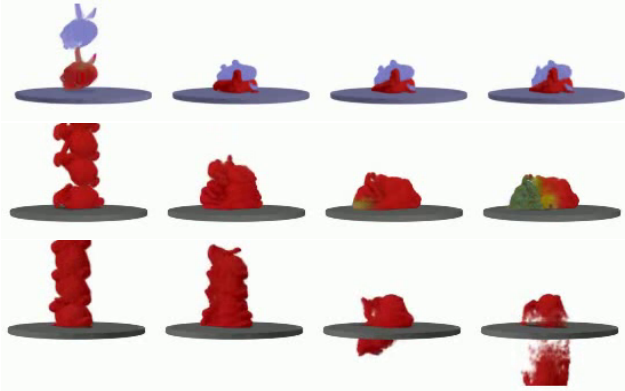


Figure 9. Although 3DGSim has not been trained on scenes containing this particular elastic object nor several objects, it predicts physically plausible deformations. Interestingly, the combined weight of five objects pushes the particles through the table causing color changes or falling particles.

interactions by duplicating bodies (2 to 5 instances, see Figure 9), and run the simulation for 180 steps. Despite being trained only on object-ground collisions, 3DGSim correctly captures realistic multi-body dynamics. Instead of collapsing into chaotic interactions, individual objects retain structural integrity and move cohesively. We attribute this to the transformer architecture, which avoids structural constraints that might limit generalization, as seen in GNN approaches.

A striking consequence of removing explicit physics biases is that 3DGSim not only captures physics but also learns to reason about broader scene properties. One particularly intriguing outcome is its ability to accurately model shadows as shown in Figure 8, which requires a holistic understanding of scene geometry, lighting, and object relationships.

### 4.3. Simulation speed

Simulation speed is critical for robotics applications. Traditional simulators (FEM, MPM, PBD) typically employ small integration timesteps. Learned approaches enable larger timesteps, allowing 3DGSim to simulate elastic, cloth at 42 FPS and rigid dynamics at 12 FPS, with inference speeds of  $\sim 16$  FPS (4 past steps) and  $\sim 20.1$  FPS (2 past steps), using under 20 GB VRAM on an H100 GPU and achieving *near real-time prediction speeds*.

## 5. Discussion

3D Gaussian simulators (3DGSim) integrate particle-based simulation with recent advancements in point-cloud transformer scalability and the fast-rendering capabilities of 3D Gaussian splatting. This combination results in an efficient and scalable simulator capable of learning complex interactions between physical particles from multi-view RGB images. By combining pooling with leveraging patch-wise

attention of temporally serialized point clouds, 3DGSim effectively mitigates the inductive biases of GNNs, which rely on local message passing or global nodes.

Furthermore, recognizing the critical role of visual scene information in simulating motion, we jointly train inverse rendering alongside dynamics. As a consequence, the model does not only learn a rich visual representation of the scene but also extracts features essential for modeling dynamics such as shadows which could be informative about relative distances.

By avoiding inductive biases where possible and prioritizing scalability over first-principles, transformers have already demonstrated their effectiveness in uncovering complex patterns within large datasets. In turn, we are eager to explore 3DGSim on significantly larger datasets encompassing a diverse range of physical interactions. As we scale up, incorporating language embeddings into simulators emerges as a particularly promising direction. After all, words such as “liquid” or “mirror” could provide meaningful priors about an object’s physical properties. In this regard, we hope that 3DGSim points the way towards scalable particle-based simulators that are able to infer the interactions of complex physical phenomena from video as well as potentially text data, paving the way for robots that truly understand the dynamics of their surroundings.

## References

- [1] Yunzhu Li, Shuang Li, Vincent Sitzmann, Pulkit Agrawal, and Antonio Torralba. 3d neural scene representations for visuomotor control. In *Conference on Robot Learning*, pages 112–123. PMLR, 2022.
- [2] Ziyi Wu, Nikita Dvornik, Klaus Greff, Thomas Kipf, and Animesh Garg. Slotformer: Unsupervised visual dynamics simulation with object-centric models, 2023.
- [3] NVIDIA, ., Niket Agarwal, Arslan Ali, Maciej Bala, et al. Cosmos world foundation model platform for physical ai, 2025.
- [4] Saman Motamed, Laura Culp, Kevin Swersky, Priyank Jaini, and Robert Geirhos. Do generative video models understand physical principles? *arXiv preprint arXiv:2501.09038*, 2025.
- [5] Yulia Rubanova, Tatiana Lopez-Guevara, Kelsey R. Allen, William F. Whitney, Kimberly Stachenfeld, and Tobias Pfaff. Learning rigid-body simulators over implicit shapes for large-scale scenes and vision, 2024.
- [6] Mahdi Saleh, Michael Sommersperger, Nassir Navab, and Federico Tombari. Physics-encoded graph neural networks for deformation prediction under contact. *arXiv preprint arXiv:2402.03466*, 2024.
- [7] Haotian Xue, Antonio Torralba, Josh Tenenbaum, Dan Yamins, Yunzhu Li, and Hsiao-Yu Tung. 3d-intphys: Towards more generalized 3d-grounded visual intuitive physics under challenging scenes. *Advances in Neural Information Processing Systems*, 36:7116–7136, 2023.
- [8] Kelsey R. Allen, Yulia Rubanova, Tatiana Lopez-Guevara, William Whitney, Alvaro Sanchez-Gonzalez, Peter



- Battaglia, and Tobias Pfaff. Learning rigid dynamics with face interaction graph networks, 2022.
- [9] Haochen Shi, Huazhe Xu, Zhiao Huang, Yunzhu Li, and Jiajun Wu. Robocraft: Learning to see, simulate, and shape elasto-plastic objects in 3d with graph networks. *The International Journal of Robotics Research*, 43(4):533–549, 2024.
- [10] William F. Whitney, Tatiana Lopez-Guevara, Tobias Pfaff, Yulia Rubanova, Thomas Kipf, Kimberly Stachenfeld, and Kelsey R. Allen. Learning 3d particle-based simulators from rgb-d videos, 2023.
- [11] William F. Whitney, Jacob Varley, Deepali Jain, Krzysztof Choromanski, Sumeet Singh, and Vikas Sindhwani. Modeling the real world with high-density visual particle dynamics, 2024.
- [12] Jiayu Wang, Jingkai Sun, Junhao He, Ziyi Zhang, Qiang Zhang, Mingyuan Sun, and Renjing Xu. DEL: Discrete Element Learner for Learning 3D Particle Dynamics with Neural Rendering, 2024.
- [13] Leonardo Barcellona, Andrii Zadaianchuk, Davide Allegro, Samuele Papa, Stefano Ghidoni, and Efstratios Gavves. Dream to manipulate: Compositional world models empowering robot imitation learning with imagination, 2024.
- [14] Eric Heiden, Ziang Liu, Vibhav Vineet, Erwin Coumans, and Gaurav S Sukhatme. Inferring articulated rigid body dynamics from rgb-d video. In *2022 IEEE/RSJ International Conference on Intelligent Robots and Systems (IROS)*, pages 8383–8390. IEEE, 2022.
- [15] Genesis Authors. Genesis: A universal and generative physics engine for robotics and beyond, 2024.
- [16] Emanuel Todorov, Tom Erez, and Yuval Tassa. Mujoco: A physics engine for model-based control. In *2012 IEEE/RSJ international conference on intelligent robots and systems*, pages 5026–5033. IEEE, 2012.
- [17] Erwin Coumans and Yunfei Bai. Pybullet, a python module for physics simulation for games, robotics and machine learning, 2016–2021.
- [18] Shital Shah, Debadepta Dey, Chris Lovett, and Ashish Kapoor. Airsim: High-fidelity visual and physical simulation for autonomous vehicles. In *Field and Service Robotics: Results of the 11th International Conference*, pages 621–635. Springer, 2018.
- [19] Russ Tedrake. Drake: Model-based design and verification for robotics, 2019.
- [20] Viktor Makoviychuk, Lukasz Wawrzyniak, Yunrong Guo, Michelle Lu, Kier Storey, Miles Macklin, David Hoeller, Nikita Rudin, Arthur Allshire, Ankur Handa, et al. Isaac gym: High performance gpu-based physics simulation for robot learning, 2021.
- [21] Yuanming Hu, Luke Anderson, Tzu-Mao Li, Qi Sun, Nathan Carr, Jonathan Ragan-Kelley, and Frédo Durand. DiffTaichi: Differentiable programming for physical simulation, 2019.
- [22] Miles Macklin. Warp: A high-performance python framework for gpu simulation and graphics, 2022.
- [23] Ben Mildenhall, Pratul P Srinivasan, Matthew Tancik, Jonathan T Barron, Ravi Ramamoorthi, and Ren Ng. Nerf: Representing scenes as neural radiance fields for view synthesis. *Communications of the ACM*, 65(1):99–106, 2021.
- [24] Bernhard Kerbl, Georgios Kopanas, Thomas Leimkühler, and George Drettakis. 3d gaussian splatting for real-time radiance field rendering. *ACM Transactions on Graphics*, 42(4), 2023.
- [25] Olaf Ronneberger, Philipp Fischer, and Thomas Brox. U-net: Convolutional networks for biomedical image segmentation. In *Medical image computing and computer-assisted intervention—MICCAI 2015: 18th international conference, Munich, Germany, October 5–9, 2015, proceedings, part III 18*, pages 234–241. Springer, 2015.
- [26] Yuedong Chen, Haofei Xu, Chuanxia Zheng, Bohan Zhuang, Marc Pollefeys, Andreas Geiger, Tat-Jen Cham, and Jianfei Cai. Mvsplat: Efficient 3d gaussian splatting from sparse multi-view images. *arXiv preprint arXiv:2403.14627*, 2024.
- [27] James H Clark. Hierarchical geometric models for visible surface algorithms. *Communications of the ACM*, 19(10): 547–554, 1976.
- [28] Jiale Xu, Weihao Cheng, Yiming Gao, Xintao Wang, Shenghua Gao, and Ying Shan. Instantmesh: Efficient 3d mesh generation from a single image with sparse-view large reconstruction models. *arXiv preprint arXiv:2404.07191*, 2024.
- [29] Alvaro Sanchez-Gonzalez, Jonathan Godwin, Tobias Pfaff, Rex Ying, Jure Leskovec, and Peter W. Battaglia. Learning to Simulate Complex Physics with Graph Networks, 2020.
- [30] Xiaoyang Wu, Li Jiang, Peng-Shuai Wang, Zhijian Liu, Xihui Liu, Yu Qiao, Wanli Ouyang, Tong He, and Hengshuang Zhao. Point transformer v3: Simpler, faster, stronger. In *CVPR*, 2024.
- [31] Jonathon Luiten, Georgios Kopanas, Bastian Leibe, and Deva Ramanan. Dynamic 3d gaussians: Tracking by persistent dynamic view synthesis. In *3DV*, 2024.
- [32] Nikhil Keetha, Jay Karhade, Krishna Murthy Jatavallabhula, Gengshan Yang, Sebastian Scherer, Deva Ramanan, and Jonathon Luiten. Splatam: Splat, track and map 3d gaussians for dense rgb-d slam. In *Proceedings of the IEEE/CVF Conference on Computer Vision and Pattern Recognition*, 2024.
- [33] Heng Yu, Joel Julin, Zoltán Á Milacski, Koichiro Niinuma, and László A. Jeni. CoGS: Controllable Gaussian Splatting, 2023.
- [34] Yi-Hua Huang, Yang-Tian Sun, Ziyi Yang, Xiaoyang Lyu, Yan-Pei Cao, and Xiaojuan Qi. Sc-gs: Sparse-controlled gaussian splatting for editable dynamic scenes. *arXiv preprint arXiv:2312.14937*, 2023.
- [35] Mingtong Zhang, Kaifeng Zhang, and Yunzhu Li. Dynamic 3d gaussian tracking for graph-based neural dynamics modeling. In *8th Annual Conference on Robot Learning*, 2024.
- [36] Yixuan Wang, Mingtong Zhang, Zhuoran Li, Tarik Kelestemur, Katherine Driggs-Campbell, Jiajun Wu, Li Fei-Fei, and Yunzhu Li. D3Fields: Dynamic 3D Descriptor Fields for Zero-Shot Generalizable Rearrangement, 2024.
- [37] Jad Abou-Chakra, Krishan Rana, Feras Dayoub, and Niko Sünderhauf. Physically Embodied Gaussian Splatting: A Realtime Correctable World Model for Robotics, 2024.
- [38] Julius Plücker. *Neue Geometrie des Raumes gegründet auf die Betrachtung der geraden Linie als Raumelement*. Teubner, Leipzig, 1868-1869.

- [39] Ashish Vaswani, Noam Shazeer, Niki Parmar, Jakob Uszkoreit, Llion Jones, Aidan N Gomez, Łukasz Kaiser, and Illia Polosukhin. Attention is all you need. In I. Guyon, U. Von Luxburg, S. Bengio, H. Wallach, R. Fergus, S. Vishwanathan, and R. Garnett, editors, *Advances in Neural Information Processing Systems*. Curran Associates, Inc., 2017.
- [40] Richard Zhang, Phillip Isola, Alexei A. Efros, Eli Shechtman, and Oliver Wang. The unreasonable effectiveness of deep features as a perceptual metric, 2018.
- [41] Laura Downs, Anthony Francis, Nate Koenig, Brandon Kinman, Ryan Hickman, Krista Reymann, Thomas B. McHugh, and Vincent Vanhoucke. Google scanned objects: A high-quality dataset of 3d scanned household items, 2022.
- [42] Tri Dao. FlashAttention-2: Faster attention with better parallelism and work partitioning. In *International Conference on Learning Representations (ICLR)*, 2024.

# Learning 3D-Gaussian Simulators from RGB Videos

## Supplementary Material

### A. Ablations

For the ablation studies, only the elastic dataset is used. The default configuration uses the latent representation, 4-step past conditioning, 12-step future rollouts, 4 input views, 5 target views, and a total of 12 cameras for training, unless otherwise specified. Any deviations from these parameters are explicitly stated or made clear within the context of the respective ablation.

This analysis provides detailed insights into design and strategic choices that inform future improvements of our approach.

#### A.1. Rollout Length.

Rollout Length	PSNR Future	PSNR Past
2 steps	26.43 $\pm$ 3.48	35.70 $\pm$ 2.51
4 steps	28.83 $\pm$ 4.96	35.25 $\pm$ 2.53
8 steps	30.64 $\pm$ 3.23	33.86 $\pm$ 2.17
<b>12 steps</b>	<b>33.15 <math>\pm</math> 3.51</b>	<b>34.55 <math>\pm</math> 2.26</b>

Table 3. Rollout Length

We evaluate the influence of prediction rollout length during training (2, 4, 8, and 12 steps). Consistent with expectations, results improve significantly as the rollout length increases, reaching a peak performance at 12 steps with a PSNR Future of 33.15  $\pm$  3.51. Extending the number of rollout steps enhances the model’s predictive capability but leads to significant memory requirements. Employing regularization methods such as random-walk noise injection or diffusion techniques or even other modality (see later) can help reduce the required rollout steps.

#### A.2. Camera Setup.

Setup	PSNR Future	PSNR Past
Explicit 3 views out of 6	21.02 $\pm$ 1.78	16.86 $\pm$ 0.83
<b>Latent 3 views out of 6</b>	<b>31.60 <math>\pm</math> 3.09</b>	<b>32.55 <math>\pm</math> 2.12</b>
<b>Latent 4 views out of 12</b>	<b>33.15 <math>\pm</math> 3.51</b>	<b>34.55 <math>\pm</math> 2.26</b>

Table 4. Camera Setup (85k steps)

To approximate a realistic scenario suitable for real-world deployment, we investigate performance with reduced camera setups. Interestingly, the latent representation models achieve robust performance even when trained with 3 views out of 6 total cameras (PSNR 33.15), whereas

explicit representation models degrade significantly (PSNR drops to 21.02) due to convergence of the encoder to poor local minima. This local minimum manifests as camera-specific overfitting, where the model erroneously predicts particle arrangements forming planar, screen-aligned shapes. While this artificially reduces the training loss of target viewpoints, it undermines the true representation quality and disrupts convergence to a consistent 3D reconstruction. Further restricting the setup to only 2 views out of 4 cameras results in unsuccessful training for both latent and explicit models, indicating that very limited camera setups demand careful placement or preliminary encoder pre-training, which should be investigated in a future work.

#### A.3. Segmentation Masks.

Segmentation	PSNR Future	PSNR Past
Without masks	32.66 $\pm$ 3.43	39.08 $\pm$ 3.18
With masks	33.15 $\pm$ 3.51	34.55 $\pm$ 2.26

Table 5. Segmentation Masks

While our final models use segmentation masks for static objects (e.g., ground surfaces), we explore training without these masks to test model reliance on explicit segmentation. We find only a slight reduction in performance (32.66 vs. 33.15), demonstrating the models’ capability to implicitly infer static scene regions directly from raw RGB inputs. Thus, explicit segmentation masks are helpful but not strictly essential.

#### A.4. Modality Configurations

Modality	PSNR Future	PSNR Past
4-1-2-6	32.59 $\pm$ 3.22	33.39 $\pm$ 2.21
4-4-1-3	31.98 $\pm$ 3.78	34.03 $\pm$ 2.39
4-1-1-12	33.15 $\pm$ 3.51	34.55 $\pm$ 2.26

Table 6. Input Modality

Different input modality configurations were tested. Here, we adapt the notation "a-b-c-d", each varying the temporal span of input conditioning  $a$  is the number of particle frames representing the state,  $b$  indicates the number of backward frames used to predict  $c$  future steps, and total rollout steps during training  $d$ , leading to  $b \cdot c \cdot d$  rollout steps per training step. Both variants ("4-1-2-6", "4-4-1-3" attain

competitive performance (PSNR of 32.59 and 32.27 respectively), significantly reducing the computational load compared to longer standard rollouts. This highlights promising avenues for future investigation, emphasizing balance between computational efficiency and performance quality.

### A.5. Grid Resolution

Grid Size	PSNR Future	PSNR Past
0.002	25.39 ± 2.95	32.28 ± 2.68
<b>0.004</b>	<b>33.15 ± 3.51</b>	<b>34.55 ± 2.26</b>
0.008	25.40 ± 3.84	30.78 ± 2.63
0.0012	24.06 ± 3.53	31.74 ± 2.56

Table 7. Grid Resolution.

We test a series of grid resolutions (0.002, 0.004, and 0.008), observing optimal results at 0.004 with a PSNR of 33.15. Both higher (0.008) and finer resolutions (0.002) degrade performance, suggesting an optimal balance achieved at 0.004 between detail preservation and computational complexity for our scene size.

### A.6. Temporal Merger.

Temporal Merger Setup	PSNR Future	PSNR Past
[1,1,2,2..] with embedding	27.55 ± 3.22	31.68 ± 2.60
[1,1,4,..] with embedding	26.79 ± 2.94	32.21 ± 2.73
[1,2,2,..] without embedding	25.07 ± 3.22	31.16 ± 2.59
<b>[1,2,2,..] with embedding (120k)</b>	<b>33.15 ± 3.51</b>	<b>34.55 ± 2.26</b>
[1,1,1,2,2] with embedding	18.87 ± 1.50	18.09 ± 1.45
[1,4,..] with embedding	18.19 ± 1.29	18.33 ± 1.48

Table 8. Temporal Merger. The models are trained for 80k steps if not specified otherwise.

We experiment with various temporal merging strides for each encoder stage combined with embedding options of timestep position encoding. Since we only train with 4 past steps, the strides “..” don’t influence the results. After 80k iterations, results clearly indicate two critical factors for success: the use of learned positional embeddings and timing of merging operations. Optimal results occur when merging temporal information only after early spatial processing stages ([1,2,2..]), whereas early or too-late merging drastically diminishes performance. Poor outcomes with late merging likely arise due to spatial pooling operations that dilute vital temporal distinctions before merging.